CHAPTER 4

RESULTS AND DISCUSSION

The simulations were run for a variety of operating parameters, including temperature, pressure, concentration, and gas inlet flow rate. The pyrolysis rate was found to be maximum at high temperatures and low pressures. The effects of Other operating parameters were also studied.

4.1 Validation of simulation results

The deposition rate and outlet CH_4 conversion obtained from the CFD model were validated against the experimental data, as shown in Fig. 4.1. The overall relative error in the deposition rate and CH_4 conversion is less than 12% and 8%, respectively. Thus, this indicates that the present model can predict the experimental trends quite accurately. However, CFD simulations are underpredicted actual performance due to several factors, including oversimplified geometries, inaccurate chemical kinetics, and numerical errors. These errors can arise from discretization limitations, solver algorithm shortcomings, and experimental challenges related to multiphase flows and coupled phenomena. Moreover, the fidelity of the CFD model was accomplished by incorporating highly accurate numerical schemes, temperature-dependent physical properties, thermal diffusion (Soret effect) and radiation effects. As a result, capturing the flow physics of the commercial CVD reactor became very computationally demanding. In this work, the sensitivity analysis of the above parameters was performed in detail. However, the fidelity of the CFD simulation that included the temperature-dependent physical properties was shown in Fig. 4.1. The effect of thermal diffusion on the velocity profile, and concentration of methane is shown in Fig. D1 and D2. It has been observed that the CFD simulation that considers temperature-dependent physical properties is ~10 % more accurate than the simulation with constant temperature-physical properties.

4.2 Effect of reactor temperature

Fig. 4.2 illustrates how the temperature field varies inside the reactor at the different set values. As the gas mixture flows through the reactor, it is rapidly heated due to convection, and a uniform temperature is achieved in the axial direction at low temperatures. The simulation

results show that significant temperature variations exist near the wall surfaces at high temperatures. This implies that the maximum local Nusselt number is near hot surfaces, and it decreases as we move away from the wall due to increased thermal boundary layer thickness. Moreover, the radial temperature distribution shows that the temperature profile is axisymmetric and uniform, except at the bottom plate. The considerable temperature variation is attributed to the entry effect. It can be inferred from the simulation results that if the deposition occurs in a reaction-limited growth regime, then the deposition rate increases with increases in the temperature. However, the non-uniform distribution of precursor/intermediate caused due to non-homogenous temperature distribution considerably affects the film uniformity.

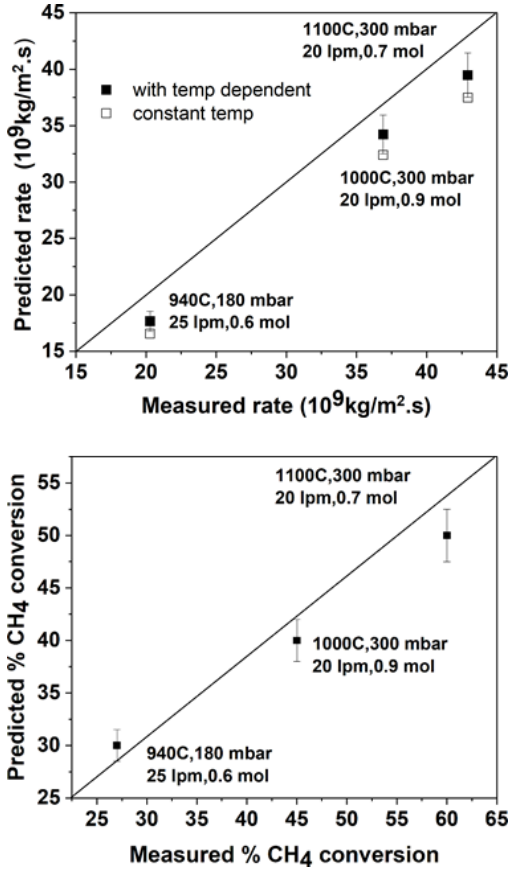

Fig. 4.1 Comparison of the model prediction of the deposition rate and exit CH_4 conversion with experimental data.

Fig. 4.3 shows the simulated cross-sectional average mole fractions of major species as a function of the reactor height at different temperatures. The vertical height mentioned in Fig. 4.3 is normalized by the total height of the four-plate substrate. The concentration (or mole fraction) values were measured as cross-sectional averages at the given horizontal plane, and

only the species with a molar fraction >10^{-4} are plotted. Several different intermediates, C_2H_2, C_2H_4, C_6H_6, and H_2 species, are formed during the pyrolysis of CH_4. A substantial difference in mole fractions was obtained at varying temperatures. Low-temperature (900°C) leads to less conversion of CH_4, and its concentration remained constant up to the middle of the reactor and then decreased slowly. It has been noted that C_2H_2 was the most abundant carbon-forming species, and the concentration of other hydrocarbons (e.g., C_2H_4 and C_6H_6), was minimal. This trend was observed for all studied temperatures. Above 900°C, the mole fractions of CH_4 rapidly diminish with increasing residence time. It is apparent that the mole fraction of C_2H_2 always increases with an increase in temperature, and it begins to be the most dominating carbon-forming species.

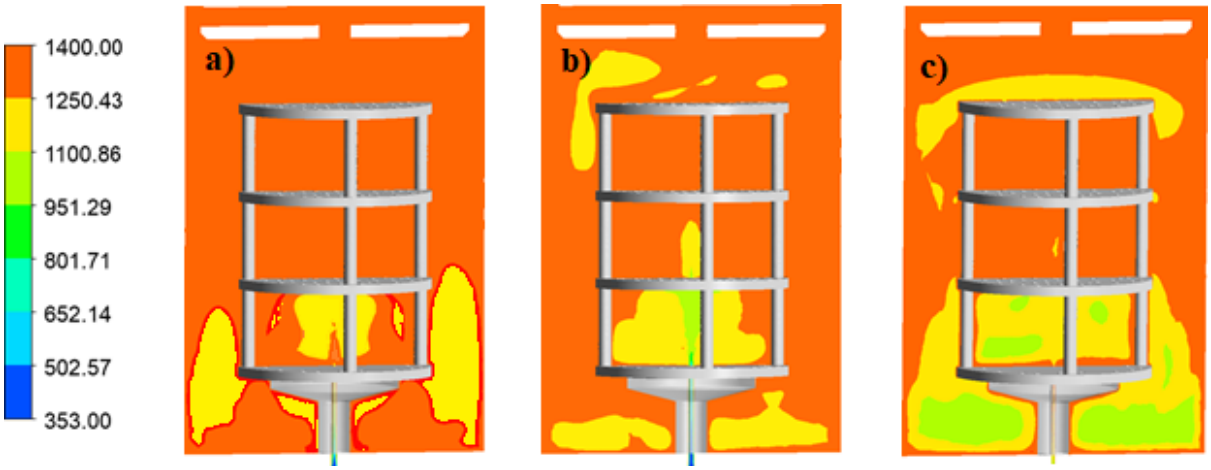

Fig. 4.2 Simulated temperature distribution at a) 900^{0}C, b) 1000^{0}C, and c) 1100^{0}C.

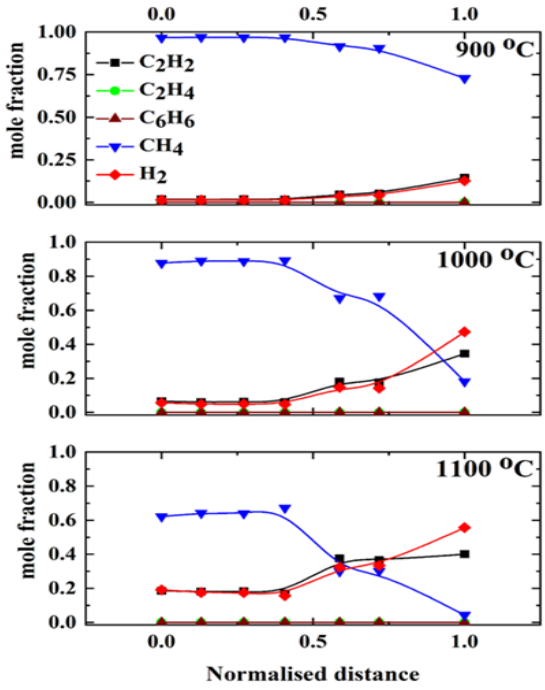

Fig. 4.3 Variation of cross-sectional averaged mole fractions of various species along the reactor length at different temperatures.

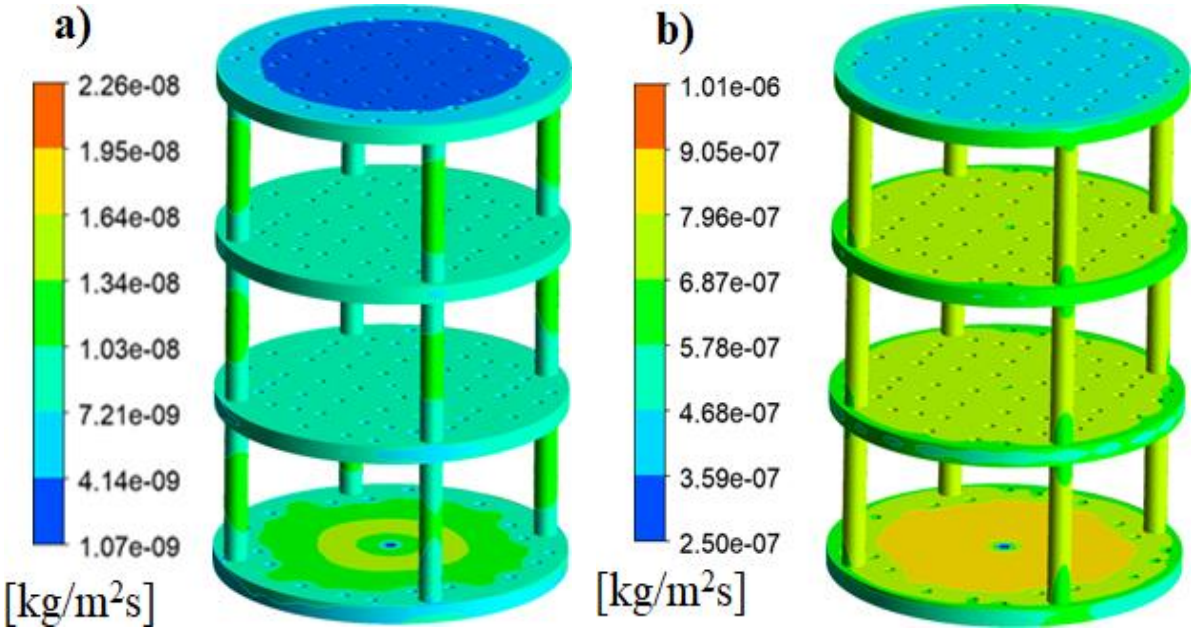

Fig. 4.4 Simulated deposition rate at reactor temperature a) 900^{0}C, and b) 1100^{0}C.

The simulated deposition profiles at 900^{0}C and 1100^{0}C are presented in Fig. 4.4. It was noticed that the film deposition rate increases with an increase in reactor temperature. However, a drastic drop in the deposition at the upper plate can be ascribed to a rise in the hydrogen

concertation at the top, inhibiting the deposition processes. Becker et al. studied carbon deposition from light hydrocarbons and observed that the carbon deposition was hindered due to the inlet H_2 concentration (Becker et al., 2000). Moreover, the species distribution in the present study unveils that C_2H_2 mainly contributes to the PyC deposition, consistent with the literature (Mankelevich and May, 2008a). The average PyC deposition rate increased from $8.75x10^{-9}$ to $7.41x10^{-7}$ kg/m^2.s when the reactor temperature rose from 900^0C to 1100^0C.

4.3 Effect of operating pressure

Fig. 4.6 depicts the distributions of C_2H_2 as a significant intermediate for PyC deposition at various pressures. It can be seen that the distribution of C_2H_2 species is axisymmetric and more homogenous at low pressure (100 mbar). The gas flow inside the reactor is controlled by forced convection. As a result, fewer circulations due to the negligible buoyancy effect were observed in the reactor at low pressure. Besides, Fig. 4.6 also illustrates how the deposition rates vary with pressures. It is evident that the deposition rate is increased with pressure. In general, the gas mixture density increases with an increase in pressure, which ultimately enhances the concentration of the C_2H_2 and decreases the concentration boundary layer thickness near the substrate. This ultimately accelerates the diffusion of C_2H_2 through the boundary layer and reacts readily at the substrate, giving rise to a higher deposition rate. However, the film uniformity is severely affected at high pressure due to the non-uniform distribution of C_2H_2, as seen in Fig. 4.5. Therefore, appropriate pressure may be used to achieve the intended growth rate and film uniformity.

The Reynolds number was calculated based on the reactor diameter, while the Grashof number was calculated using the vertical distance from the first plate. A cross-sectional average of velocity and concentration was used to estimate the various dimensionless numbers. The difference between the inlet temperature and the averaged temperature at a given cross-sectional position was used to calculate the Grashof number. The Gr/Re^2 is used to study the relative strength of natural convection compared to forced convection. It was observed that the deposition rate increased with an increase in operating pressure. However, the uniformity index decreased at higher pressures due to buoyancy-driven flow within the reactor. At high pressures (above 250 mbar), significant circulation between the wall and substrate was observed, leading to non-uniform reactant distribution and a decrease in uniformity index. Fig. 4.6 shows the variation of Gr/Re^2 ratio at different operating pressures. The Gr/Re^2 ratio increased with increasing reactor pressure, confirming the dominance of buoyancy-driven flow at high

pressures. Extensive flow recirculations were noticed around the substrate at high pressure as shown in Fig 4.6. This consequently results in considerable variation in the concentration of C_2H_2, thereby affecting the film uniformity. These findings are consistent with the dimensionless (Gr/Re^2) ratio, implying the relative magnitude of buoyancy force over the inertial force. The low Gr/Re^2 ratio is manifested at low pressure, suggesting less buoyancy-driven flow, and the strength of the flow circulations diminishes. A detailed analysis of buoyancy flow in a hot-wall CVD reactor can be found in our previous study (Deivendran et al., 2020).

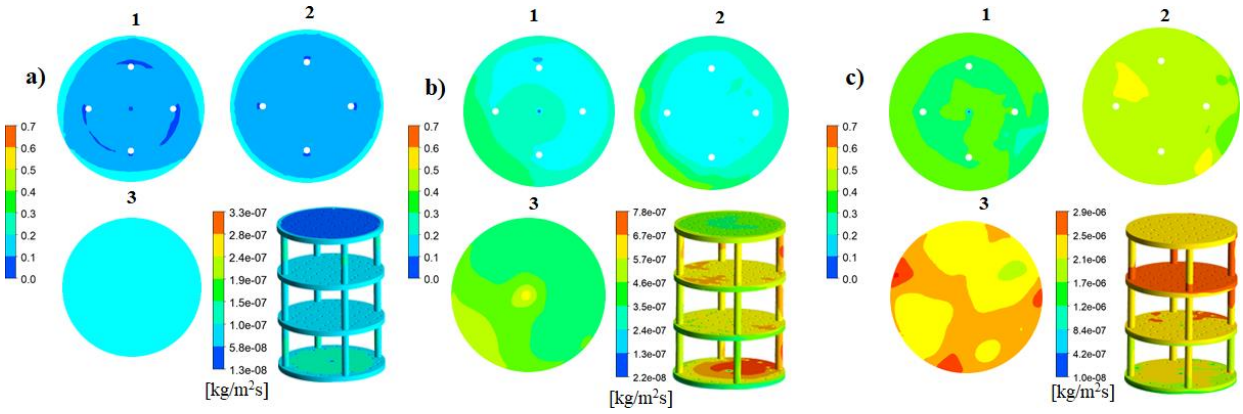

Fig. 4.5 Variation of mole fraction of C_2H_2 at different cross-sections of the reactor and deposition rate on the substrate at a) 100 mbar, b) 250 mbar, and c) 500 mbar.

The effect of pressure on the cross-section average mole fractions of all dominant species is shown in Fig. 4.5. These three cross-sections were taken in the middle of two substrates in a horizontal plane. It is apparent that the operating pressure significantly influences CH_4 conversion, increasing with an increase in reactor operating pressure. C_2H_2 is the dominant carbon forming in the reactor, and the mole fractions of C_2H_4 and C_6H_6 are negligible compared with C_2H_2 for all studied pressures. The CH_4 is immediately pyrolysed at an inlet at high pressure, and its mole fraction drastically decreases in the reactor. On the other hand, the C_2H_2 mole gradually increases from the inlet towards the exit of the reactor.

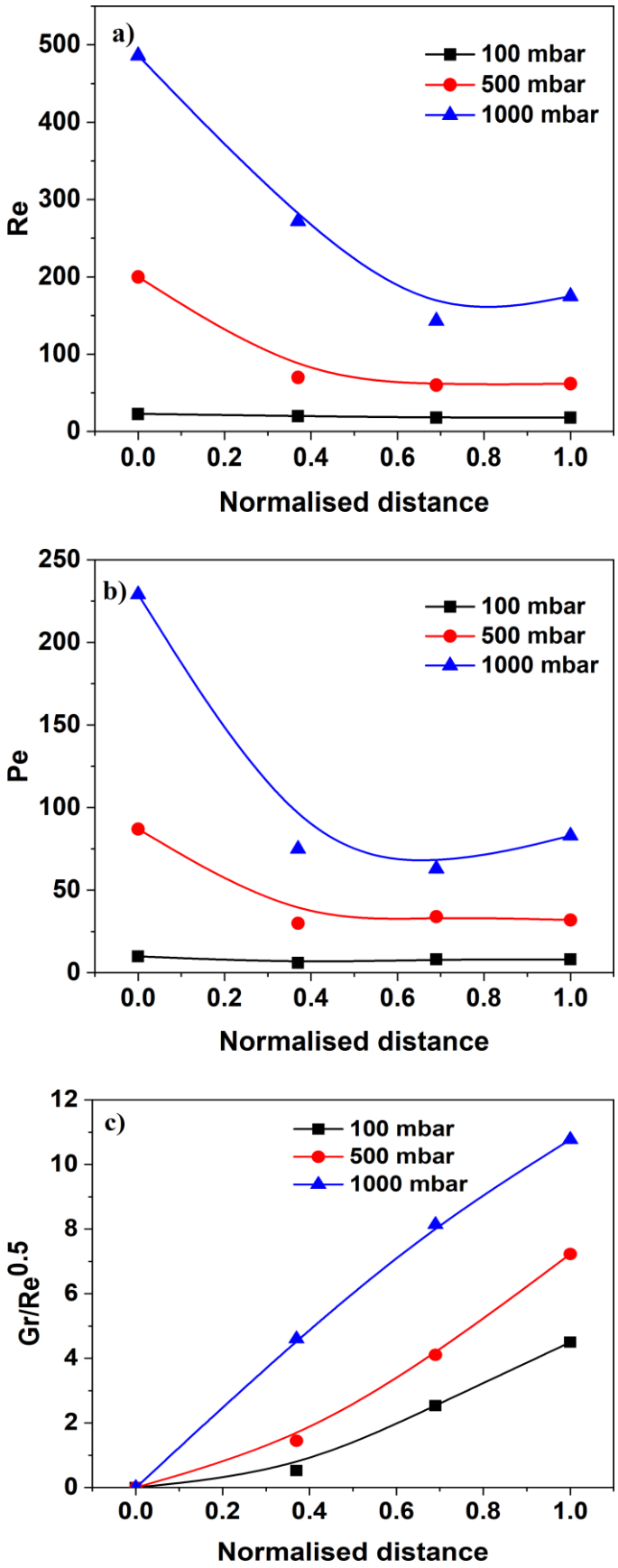

Fig. 4.6 Distribution of various dimensionless numbers at different operating pressures.

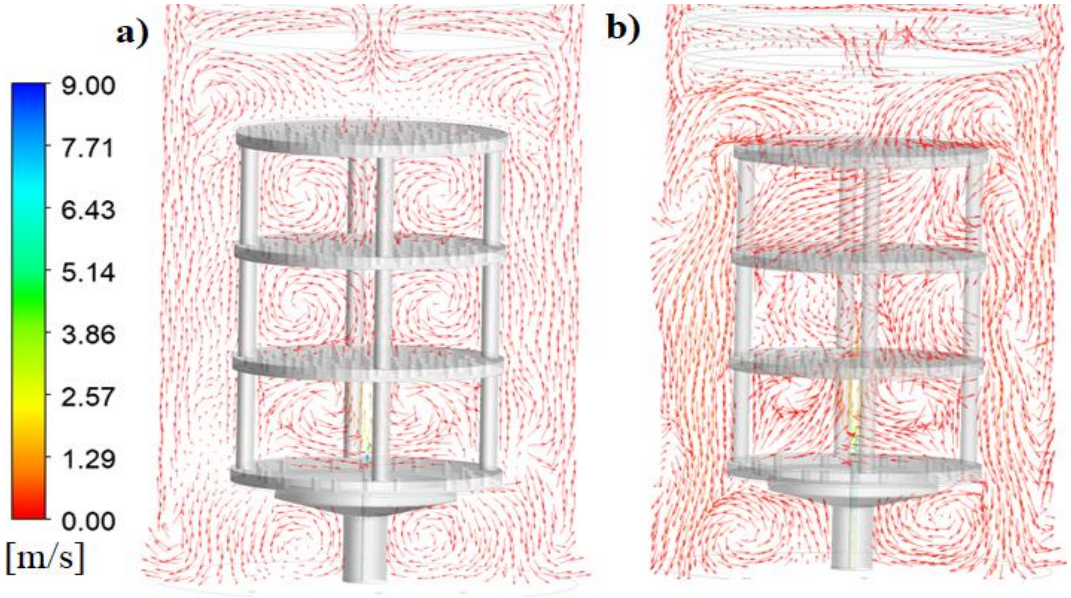

Fig. 4.7 Velocity vectors near the substrate at a) 100 mbar, b) 500 mabr and c) 1000 mbar, respectively.

4.4 Effect of total flow rate

The total flow rate was changed in the range of 10-30 standard litre per minute (slm) (hardware limitation of the reactor) to study its effect on the film quality. With increasing the flow rate, the cold gas flow is penetrated further into the reactor and reduces the temperature of the surrounding areas as shown in Fig.4.8. However, the thermal boundary layers near the substrate are still uniform. The simulation results reveal that the inlet flow rate increase does not significantly affect the reactor hydrodynamics. There are always recirculations present in the reactor, but the size of the recirculation slightly diminishes due to reduced buoyancy force at 30 slm. Fig. 4.10 shows the C_2H_2 concentration and deposition rate profiles at different flow rates. It can be seen that the mole fraction of C_2H_2 remained unchanged in both cases, indicating that the pyrolysis of CH_4 is not affected by flow rate, and similar deposition rates were achieved in both cases. However, a slightly high film uniformity was obtained at 30 slm owing to the uniform concentration of C_2H_2. Therefore, the simulation results disseminate that the effect of flow rate on film performance is feeble.

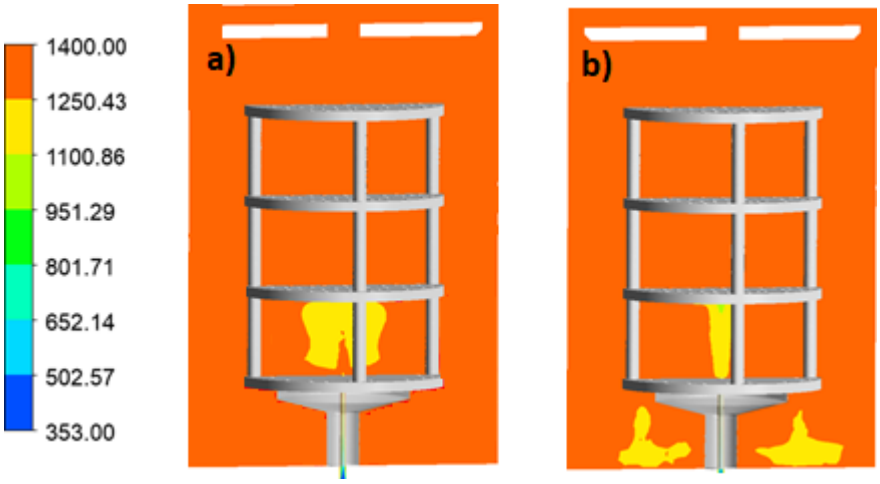

Fig. 4.8 Temperature profile at a) 10 slm, and b) 30 slm, respectively.

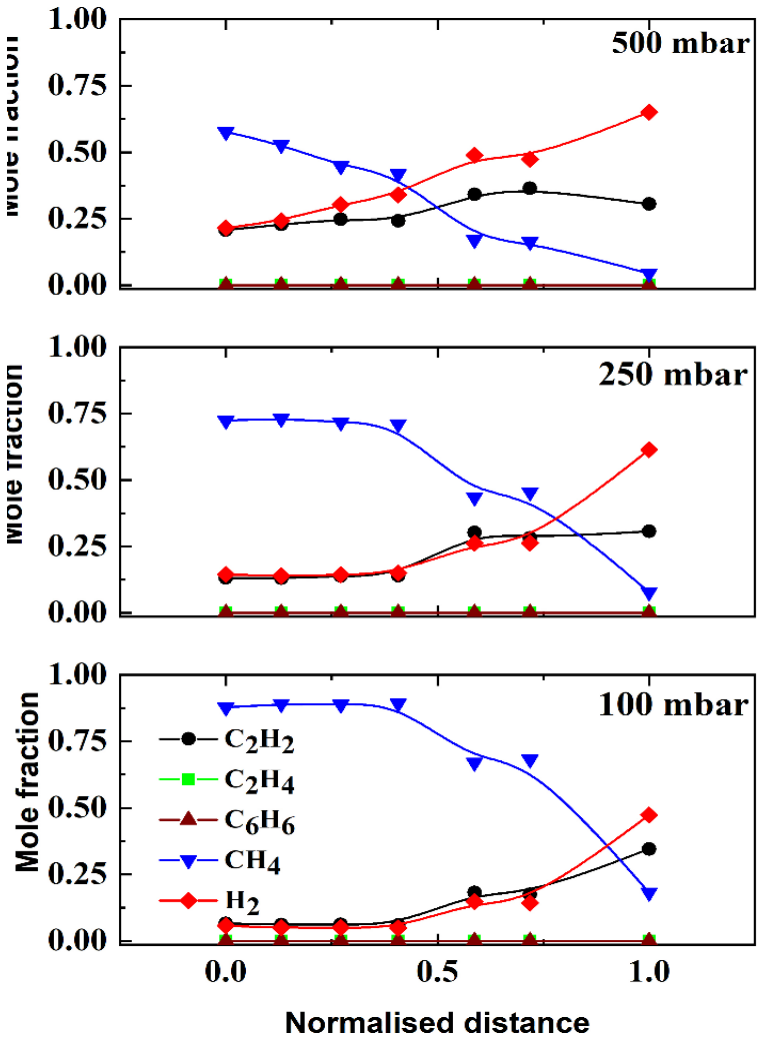

Fig. 4.9 Variation of cross-sectional averaged mole fractions of various species along the reactor length at different temperatures.

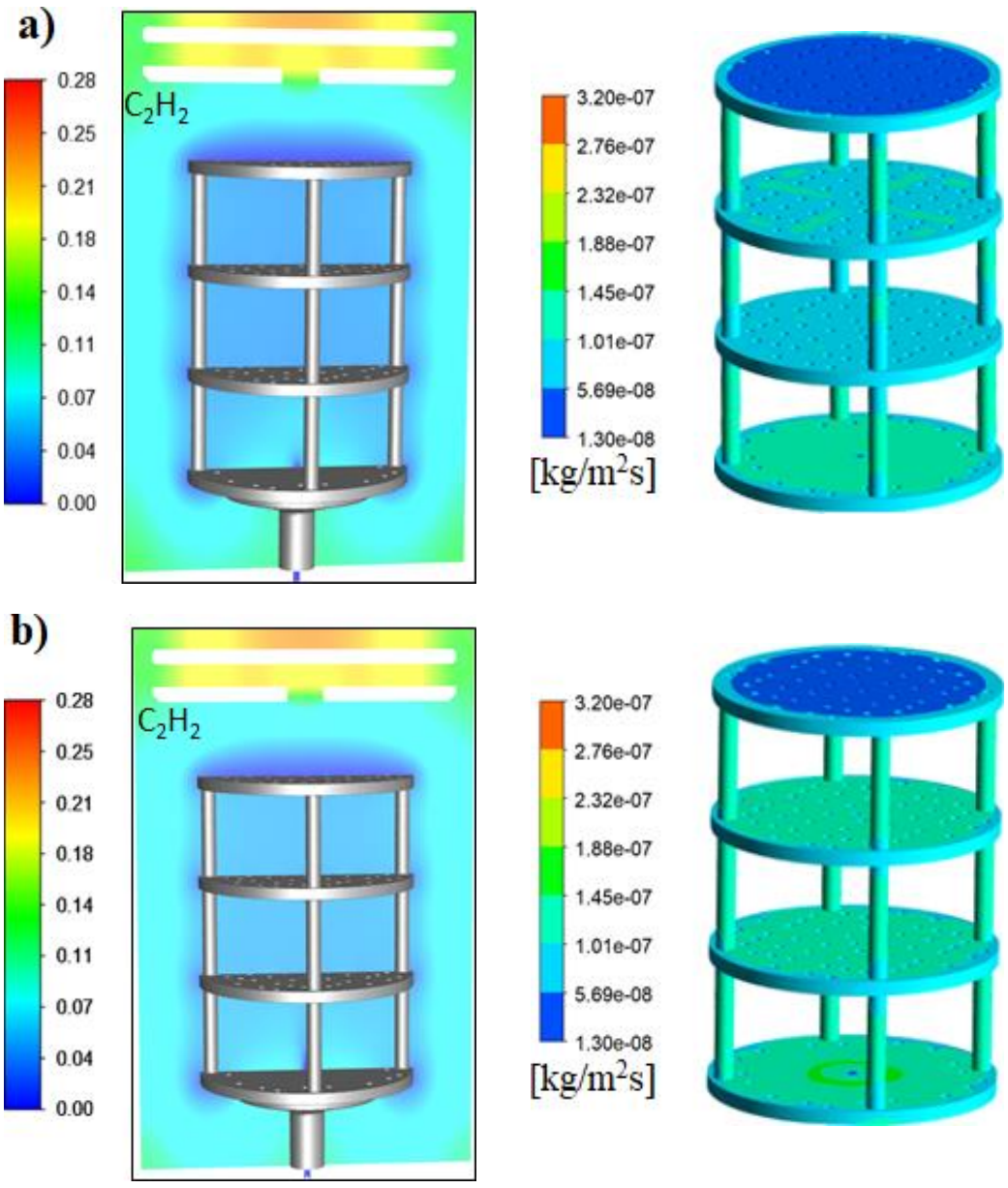

Fig. 4.10 Variation of mole fraction of C_2H_2 species along the reactor length and deposition rate at a) 10 slm, b) 30 slm.

4.5 Effect of CH_4 mole fraction

The effect of the CH_4 mole fraction on the PyC deposition and film uniformity is described in Fig. 4.11. The CH_4 mole fraction was varied from 0.2 to 1, keeping all other parameters constant. Since the thermal conductivity (molecular diffusivity) of H_2 is high, the temperature and concentration distribution inside the reactor significantly improve on the addition of H_2 in the feed. The simulation results manifest that increasing the inlet CH_4 mole

fraction causes an increase in the PyC growth rate up to 0.7, and it decreases on further increasing the inlet CH_4 mole fraction. It can be argued that C_2H_2, being heavy, prefers to stay away from the hot substrate due to the thermophoresis effect at low inlet CH_4 mole fraction. On the other hand, an excess CH_4 prevents C_2H_2 from diffusing homogeneously over the substrate, resulting in a low deposition at a high CH_4 inlet mole fraction. Besides, the CH_4 conversion and concentration of C_2H_2 are almost identical for all CH_4 inlet mole fractions, as seen in Fig. 4.11. However, the distribution of C_2H_2 is mainly dependent on the inlet CH_4 mole fraction. The uniform concentration of C_2H_2 over the substrate was observed at 0.7 CH_4 mole fraction, which resulted in high film uniformity. The summary of the parametric effect on the film performance is depicted in Table 4.1.

Table 4.1 The summary of the parametric effect on the film performance.

Parameters	**Effects**
Pressure	Forced convection dominated gas flow at low pressure (fewer flow recirculations), C_2H_2 is the most abundant carbon forming species, Homogenous distribution of C_2H_2 species at low pressure, increase in the deposition rate with pressure, However, the film uniformity severely affected at high pressure due to the non-uniform distribution of C_2H_2.
Temperature	Significant temperature variations at high temperatures due to entry effect, increase in the C_2H_2 mole fraction with temperature, Reaction-limited growth regime (900-1100 ^{0}C), Increase in the deposition rate with temperature, film uniformity is affected at high temperature due to non-uniform distribution of C_2H_2.
CH_4 mole fraction	Improvement in the C_2H_2 distribution on the addition of H_2 in the feed, Excess CH_4 prevents homogeneous diffusion of C_2H_2, Maxima in the deposition rate, Uniform concentration of C_2H_2 over the substrate at 0.7 CH_4 mole fraction, resulting in high film uniformity.
Total flow rate	Inlet flow rate does not affect the reactor hydrodynamics, slightly low buoyancy force at the high flow rate, pyrolysis of CH_4 is not affected by flow rate, and similar deposition rates, a slightly high film uniformity at a high flow rate.

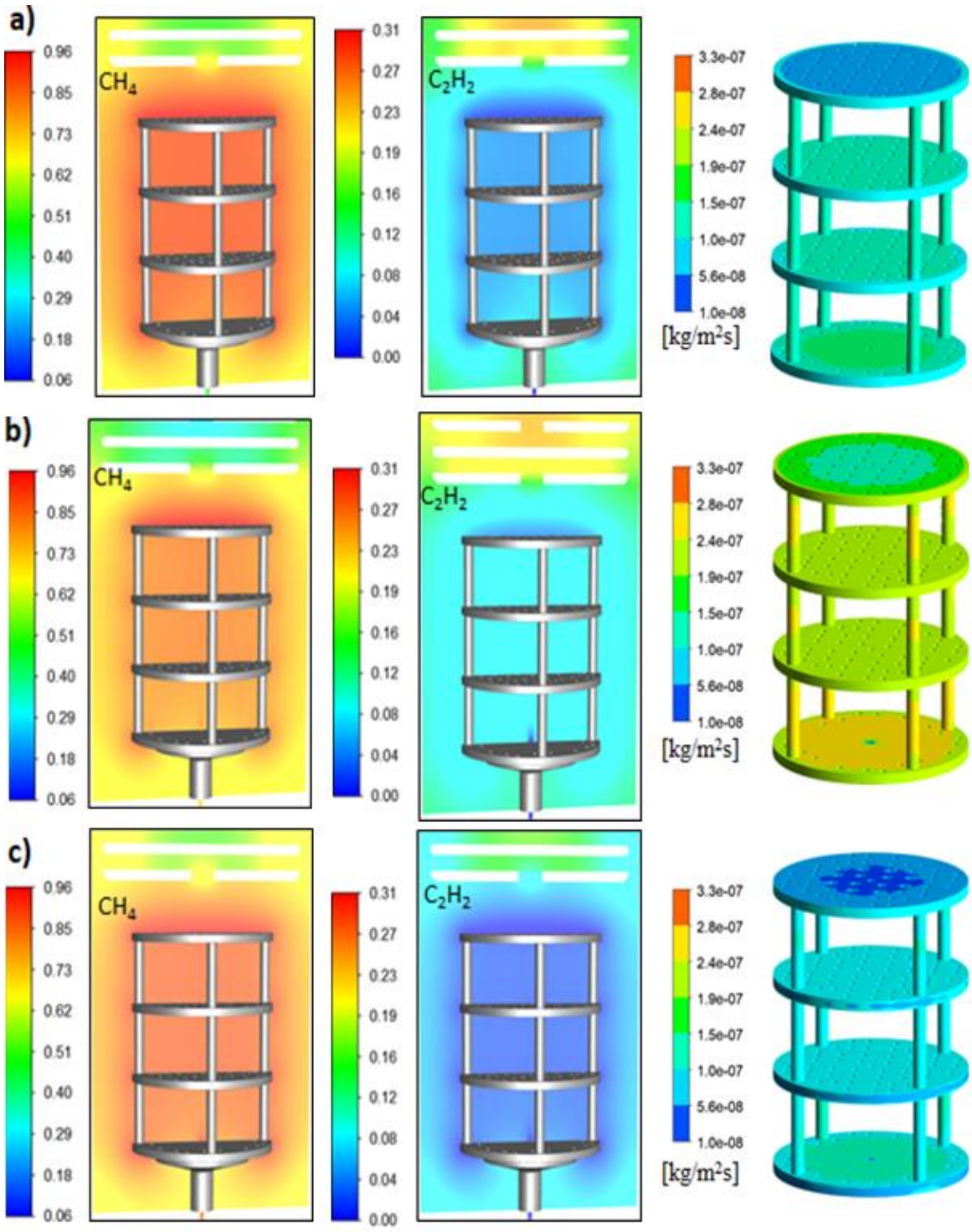

Fig. 4.11 Variation of mole fraction of CH_4 and C_2H_2 species along the reactor length and deposition rate at a) 0.5, b) 0.7, and c) 0.9 inlet mole fraction of CH_4.

4.6 Optimisation of the CVD reactor

Exploratory data analysis revealed that deposition rate was highly correlated with pressure and slightly with temperature. Contrarily, the uniformity index was strongly dependent on temperature and slightly on pressure: the combined deposition rate and uniformity depended on pressure and temperature. Fig. 4.12, 4.13 and 14 presents 2-D contour plots of how the deposition rate uniformity and combined vary with any two parameters involving total flow rate, temperature, pressure, and inlet CH_4 mole fraction. It is apparent that operating parameters have a coupling effect on the PyC deposition and film uniformity. Finally, the PyC deposition rate, uniformity, and combined (y in Eq.17) were modelled as a function of operating parameters.

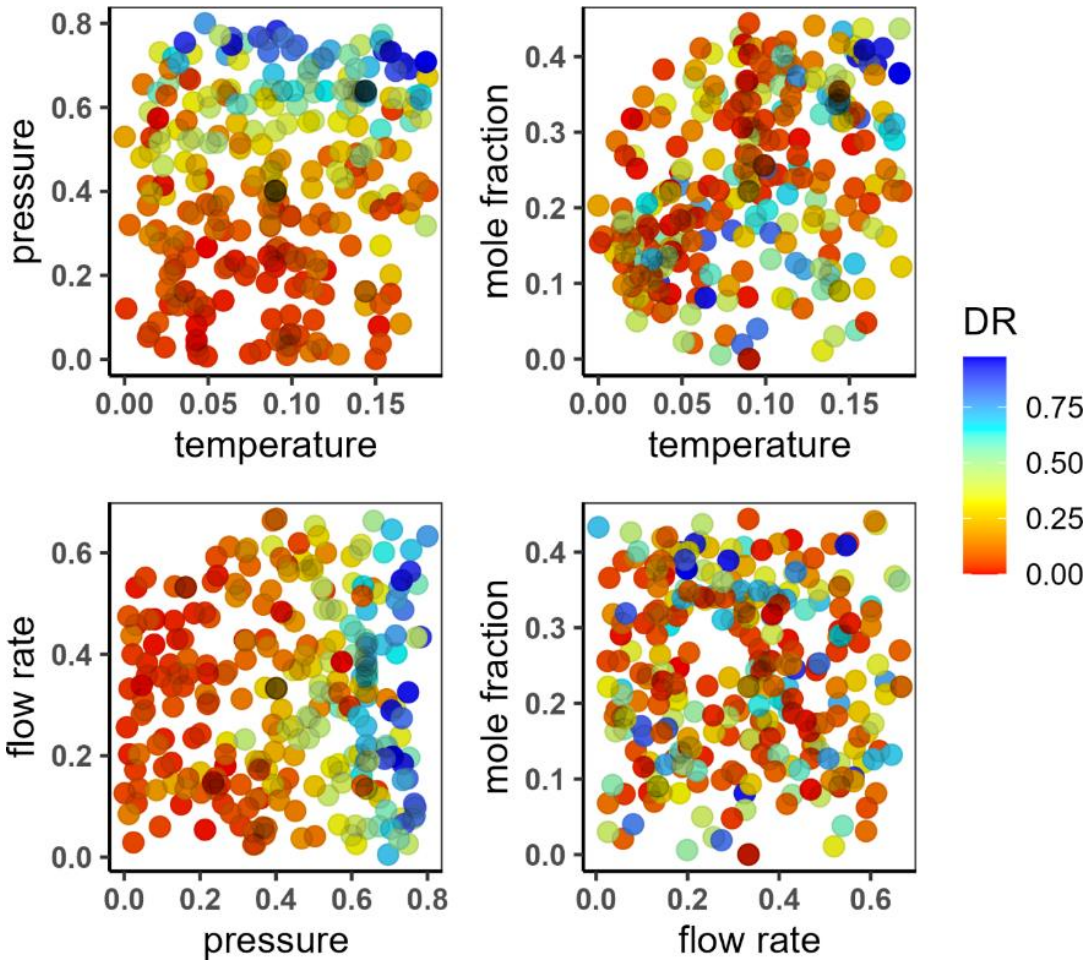

Fig. 4.12 2-D contour plots for deposition rate with two operating parameters.

The SVM algorithm was availed to envisage the deposition rate and uniformity both individually at different operating conditions. The performance of the SVM for each case is presented in Table 4.2. The performance of the SVM model via the parity plots (i.e., predicted vs. observed) for both deposition rate, uniformity index and combination of both are shown in

Fig. 4.13. There are two parity plots, one for deposition rate and one for uniformity index, both predicted using an SVM algorithm. Ideally, the data points would fall on the line y=x, which would indicate that the predicted values are perfectly accurate. However, in both plots, there is some scatter around the line y=x. This indicates that the SVM algorithm is not perfectly accurate, but it is still making relatively good predictions. The scatter is slightly more pronounced in the plot for the uniformity index, which suggests that the SVM algorithm is better at predicting the deposition rate than the uniformity index.

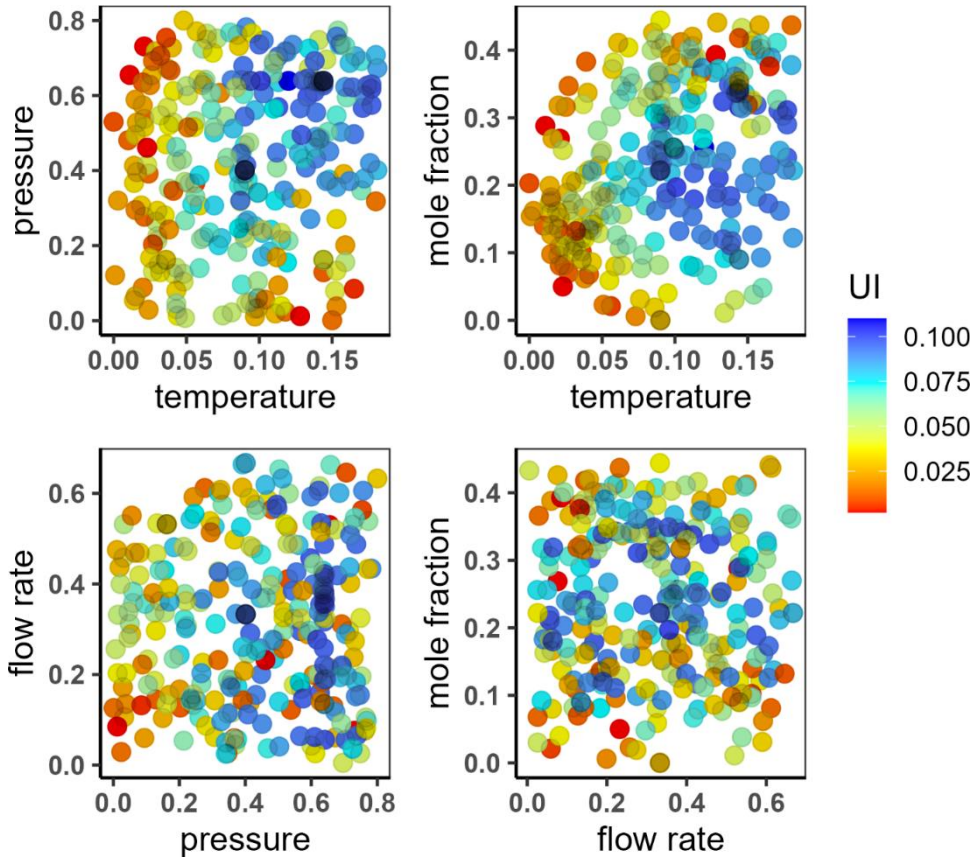

Fig. 4.13 2-D contour plots for uniformity index with a combination of two operating parameters.

Deposition rate: The deposition rate plot shows that the SVM algorithm is generally overestimating the deposition rate. This is because the predicted values tend to fall above the line y=x. However, the overestimation is not very large, and the overall correlation between the actual and predicted values is good.

Uniformity index: The uniformity index plot shows that the SVM algorithm is underestimating the uniformity index at low values and overestimating it at high values. This is because the predicted values tend to fall below the line y=x at low values and above the line

y=x at high values. However, the underestimation and overestimation are not very large, and the overall correlation between the actual and predicted values is still good.

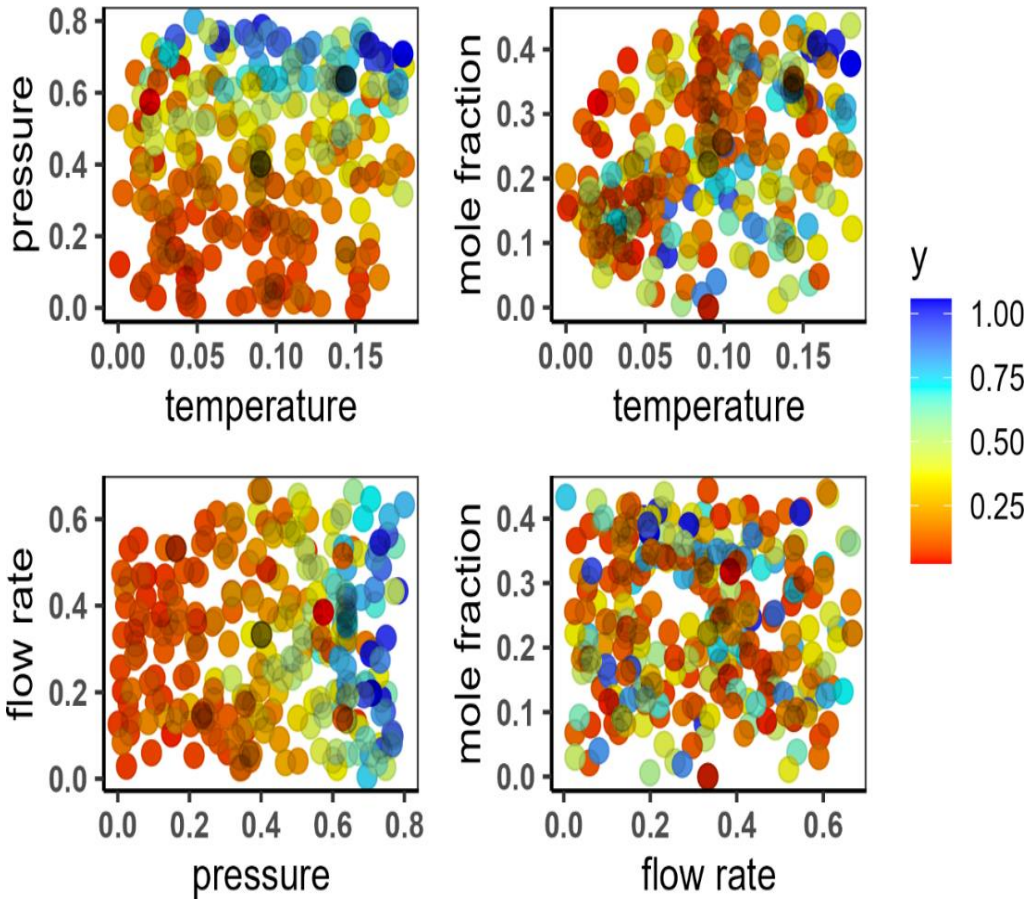

Fig. 4.14 2-D contour plots for combining the deposition rate and uniformity index with a combination of two operating parameters

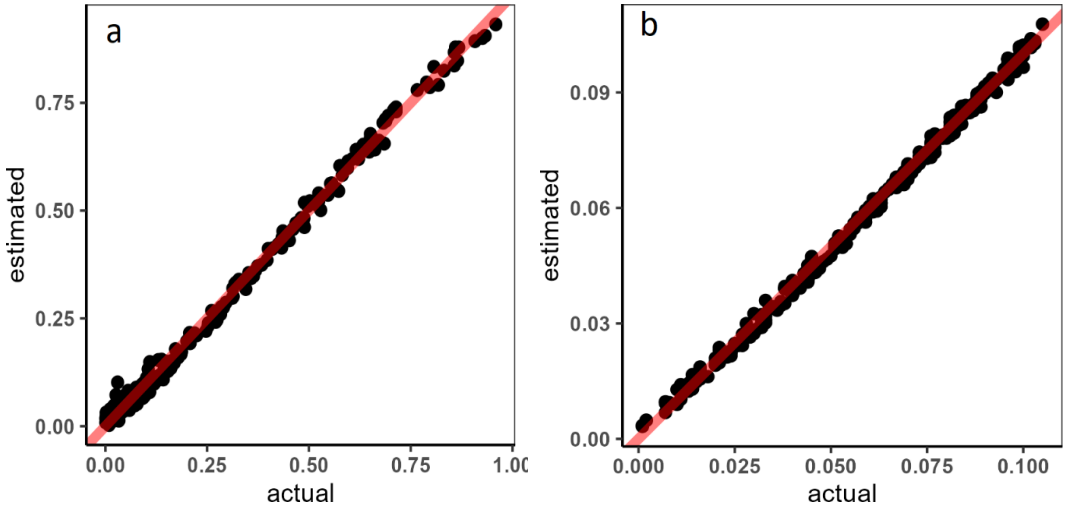

Fig. 4.15 Parity plot of predicted values versus the original values for a) deposition rate and b) uniformity index using SVM algorithm.

Apart from this, the machine learning models listed below were also trained. Before running any model, the data was separated into 'training' and 'testing' sets. A training strategy based on repeated cross-validation was used. Resampling was conducted five times with ten iterations each. The same random seed was used before running each model. It is clear that the SVR envisages the deposition and uniformity index rate with process parameters relatively well. Below is the graphical depiction of the table showing various comparisons. The linear regression model (R^2=0.64) was less accurate as compared to SVM (R^2=0.88). As already discussed in Chapter 3, the proposed strategy integrates the CFD analysis, the SVM model, and NM algorithms into a unified framework to optimise the CVD process. The optimum conditions of the CVD reactor are presented in Table 4.3.

Table 4.2 The comparison of model SVM algorithm performance to predict the simulated data

Model	RMSE	R^2	MAE
Deposition rate (DR)	0.017	0.996	0.0142
Uniformity index (UI)	0.0017	0.997	0.0014

Table 4.3 The performance of various statistical and machine learning models predicting deposition rate.

Model	Type	RMSE	R-squared	MAE
SVM	ML	0.0514	0.8867	0.0375
Boosted Tree	ML	0.0516	0.8832	0.0384
Cubist	ML	0.0516	0.8791	0.0387
Regression Tree	ML	0.0525	0.8771	0.0393
Rpart	ML	0.0548	0.8111	0.0419
Tree Bag	ML	0.0574	0.7906	0.0427
Earth	ST	0.0601	0.6718	0.0461
Neural Networks	ML	0.0617	0.6781	0.0457
PLS	ST	0.0623	0.6578	0.0455
Lasso	ST	0.0627	0.6441	0.0458
Linear Reg	ST	0.0627	0.6441	0.0458

ST = Statistics, ML = Machine Learning.

Table 4.4 The obtained optimal operating conditions for high growth and film uniformity in the CVD reactor.

Case	Temp (^{0}C)	Pressure (mbar)	Flow rate (slm)	% inlet CH_4	Deposition rate (y_1) $\times 10^{-9}$ (kg/m^2.s)	Uniformity Index (y_2)
α=1, β=1	1082	462	27	0.57	262	0.96
α=100, β=1	1082	462	27	0.57	258	0.96
α=10, β=1	1088	500	27	0.5	252	0.93
α=1, β=10	997	415	14	0.78	275	0.97
α=0.1,β=10	1082	462	27	0.57	258	0.96

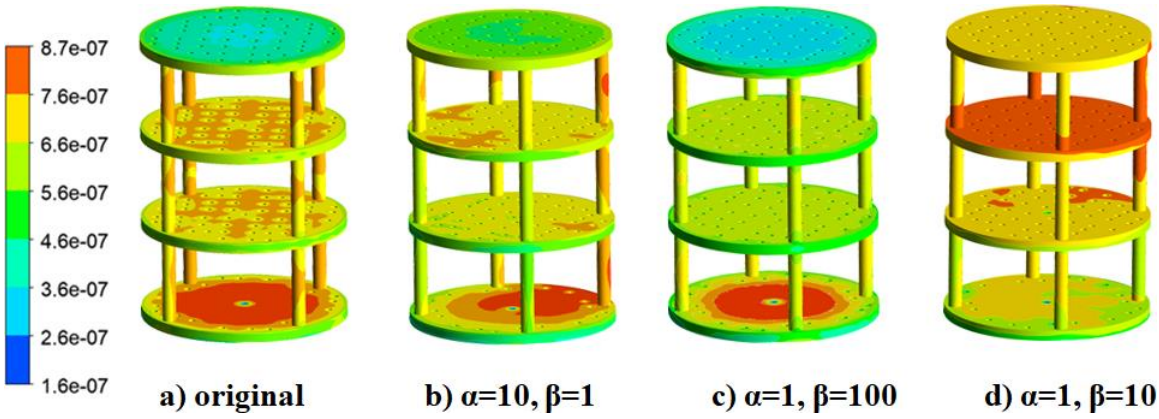

Fig. 4.16 Comparison of the uniformity index to the original operating parameters with optimum conditions from Table 4.3.

No convergence problem was encountered during the optimisation. It was observed that the fitted function (Eq. (17)) increases considerably initially and then grows slowly in the subsequent iterations. Therefore, it is evident that the combined SVM and NM algorithms efficiently locate the maxima. The advantage of the present methodology over the traditional optimisation techniques (e.g., Sequential quadratic programming) is high accuracy, computational efficiency, and easy convergence. Moreover, the CVD process is very complex; as a result, finding the analytical form of the objective function concerning the process

variables needs many trials and tremendous experience. Pareto optimality also indicates that the operating parameters cannot be assigned to make deposition rate more desirable without making film uniformity undeniable. Fig. 4.16 compares the uniformity index under the original operating conditions (Table 4.3) to those proposed in the optimized conditions. The results clearly demonstrate that the deposition uniformity is significantly enhanced by the optimized parameters. Therefore, combining the machine learning algorithm with the robust optimisation technique is advantageous for optimising complex CVD processes.

References

1. Becker, A., Hu, Z., Hüttinger, K. J., 2000. Hydrogen inhibition model of carbon deposition from light hydrocarbons. Fuel. 79, 1573-1580. https://doi.org/10.1016/S0016-2361(00)00030-2
2. Mankelevich, Y. A., May, P. W., 2008. New insights into the mechanism of CVD diamond growth: single crystal diamond in MW PECVD reactors. Diamond Relat. Mater. 17, 1021-1028. https://doi.org/10.1016/j.diamond.2008.03.022
3. Deivendran, B., Shinde, V. M., Kumar, H., Prasad, N. E. 2021. 3D modelling and optimisation of sic deposition from CH_3SiCl_3/H_2 in a commercial hot-wall reactor. J. Cryst. Growth. 554, 125944. https://doi.org/10.1016/j.jcrysgro.2020.125944